Recovering 3D clustering information with angular correlations

Jacobo Asorey,[1]⋆ Martin Crocce,[1] Enrique Gaztañaga[1] and Antony Lewis[2]

[1]*Institut de Ciències de l'Espai (IEEC-CSIC), E-08193 Bellaterra, Barcelona, Spain*
[2]*Department of Physics & Astronomy, University of Sussex, Brighton BN1 9QH*

ABSTRACT

We study how to recover the full 3D clustering information of $P(\boldsymbol{k}, z)$, including redshift space distortions (RSD), from 2D tomography using the angular auto- and cross-spectra of different redshift bins $C_\ell(z, z')$. We focus on quasi-linear scales where the minimum scale $\lambda_{\min}$ or corresponding maximum wavenumber $k_{\max} = 2\pi/\lambda_{\min}$ is targeted to be in the range $k_{\max} = \{0.05-0.2\}\, h\, \mathrm{Mpc}^{-1}$. For spectroscopic surveys, we find that we can recover the full 3D clustering information when the redshift bin width Δz used in the 2D tomography is similar to the targeted minimum scale, i.e. $\Delta z \simeq \{0.6-0.8\}\, \lambda_{\min} H(z)/c$ which corresponds to $\Delta z \simeq 0.01-0.05$ for $z < 1$. This value of Δz is optimal in the sense that larger values of Δz lose information, while smaller values violate our minimum-scale requirement. For a narrow-band photometric survey, with photo-z error $\sigma_z = 0.004$, we find almost identical results to the spectroscopic survey because the photo-z error is smaller than the optimal bin width $\sigma_z < \Delta z$. For a typical broad-band photometric survey with $\sigma_z = 0.1$, we have that $\sigma_z > \Delta z$ and most radial information is intrinsically lost. The remaining information can be recovered from the 2D tomography if we use $\Delta z \simeq 2\sigma_z$. While 3D and 2D analyses are shown here to be equivalent, the advantage of using angular positions and redshifts is that we do not need a fiducial cosmology to convert to 3D coordinates. This avoids assumptions and marginalization over the fiducial model. In addition, it becomes straightforward to combine RSD, clustering and weak lensing in 2D space.

Key words: cosmological parameters – large-scale structure of Universe.

1 INTRODUCTION

In recent years, galaxy redshift surveys have provided new information about the cosmological model of our Universe, in pace with precision cosmology from other probes like cosmic microwave background and Type Ia supernovae (Komatsu et al. 2011). We are now entering exciting times for cosmology, when surveys will go deeper and wider with increasing number of galaxy positions in each catalogue. With deep surveys we can use weak lensing (WL) information to improve constraints on cosmological parameters and also trace directly the dark matter distribution at large scales. Theoretical analysis of WL is usually made through a 2D (angular) analysis of the measured galaxy shear maps. Future surveys will have less shot noise, allowing for more freedom in how we break the sample into multiple redshift shells, so that galaxy correlations can also be measured in and between shells. In measuring angular correlations, we are projecting all the radial information within each redshift bin. But if we are able to use very thin radial shells, we can possibly recover the radial information using the angular

cross-correlations between all the redshift bins (see Montanari & Durrer 2012 for a related idea). This is what we want to investigate in this paper.

This goal is also connected to recent studies of galaxy surveys using a combination of redshift space distortions (RSD) and WL galaxy–shear and shear–shear correlations. These allow measurements of galaxy bias and the breaking of degeneracies between growth history and cosmic history, as has been recently proposed (Cai & Bernstein 2012; Gaztañaga et al. 2012). RSD are usually studied in 3D, which complicates a joint analysis with WL which is usually 2D (see Kitching, Heavens & Miller 2011 for a comparative analysis with 3D cosmic shear). If we could study RSD in 2D without loss of information, then it would be possible to do a joint analysis of both probes using only angular correlations with the corresponding simplification in the covariance analysis.

Observations directly probe redshifts and angular coordinates on the sky. Doing an angular analysis therefore does not require any prior knowledge of the cosmological model, while for doing 3D analysis we have to assume a fiducial cosmology to convert to comoving spatial coordinates. This then requires modelling the Alcock–Paczynski effect when fitting different models to our observables (Alcock & Paczynski 1979). As the transformation is

⋆E-mail: asorey@ieec.uab.es

redshift dependent one has to make sure that this procedure is not biasing the parameter constraints. If the theoretical prediction for the correlations in angle and redshift can be calculated for each model, an angular analysis relating directly to the observables is much more direct.

The final goal of this paper is to analyse the bin optimization that allows us to recover the 3D constraints on clustering using a 2D tomographic approach. We have studied this in the framework of several idealized surveys: a spectroscopic survey in a redshift range similar to the SDSS redshift range (Blake et al. 2007; Padmanabhan et al. 2007; Thomas et al. 2010); a survey with photometric redshifts from a camera with narrow-band filters like the camera used in the Physics of the accelerating Universe (PAU) survey[1] (Casas et al. 2010); and finally, a survey with redshifts obtained from photometry with broad-band filters, in a redshift range similar to Dark Energy Survey (DES).[2] For the three surveys we have analysed a bias fixed model, constraining Ω_m. In addition, in the spectroscopic survey we have also studied the standard RSD constraints on the bias b and growth index γ.

In Section 2 we describe galaxy surveys, parameters considered in the analysis and a description of the observables. In Section 3 we show the constraints obtained in our analysis for the different surveys described above. Finally, we summarize all the results in Section 4 with the conclusions.

2 METHODOLOGY

The goal of this paper is to show under which conditions, if any, one can recover the full 3D clustering information from a tomography study. By this we mean a combination of all the auto- and cross-angular spectra after the survey volume has been divided into a set of consecutive redshift bins. The angular spectra within each bin will include information mainly from transverse modes, while cross-correlations between different shells account for radial modes with scales comparable to the bin separation.

We investigate this idea in the context of a spectroscopic survey as well as two photometric surveys with different accuracies in the redshift determination. In what follows we describe these 'typical' surveys, the assumed galaxy samples, the observables considered and the figures of merit (FoMs) used to compare 3D and 2D tomography results.

Throughout the paper we used CAMB_SOURCES[3] (Lewis, Challinor & Lasenby 2000; Lewis & Challinor 2007; Challinor & Lewis 2011) to compute the matter 3D power spectra as well as the angular power spectra, including cross-correlations between radial bins.

2.1 Fiducial surveys and galaxy samples

In this section we describe our fiducial surveys and galaxy samples. We characterize them by a redshift range, a given accuracy of redshift measurements, a galaxy redshift distribution and bias.

In all cases we assume a full-sky coverage. In ideal conditions this implies that the covariance matrix of observables such as C_ℓ is diagonal in ℓ (but note that this assumption is not expected to change the conclusions of this paper). In all three surveys the overall redshift

Table 1. Comoving galaxy number densities at $z = 0.55$ assumed in this paper for the spectroscopic and narrow-band photometric surveys. Case 1 corresponds to a low shot noise level ($nP_{gal} \sim 2$ per cent, where P_{gal} is the monopole of the galaxy spectrum at $z = 0.55$ and $k = 0.1 \, h \, \mathrm{Mpc}^{-1}$) while case 2 corresponds to a high shot noise level ($nP_{gal} = 10$ per cent).

Case	$n(r) \, (h^3 \, \mathrm{Mpc}^{-3})$
Low shot noise	3.14×10^{-3}
High shot noise	6.89×10^{-4}

distribution of galaxies per square degree is taken as

$$\frac{\mathrm{d}N}{\mathrm{d}z \, \mathrm{d}\Omega} = N_{gal} \left(\frac{z}{0.55} \right)^2 \mathrm{e}^{-\left(\frac{z}{0.55} \right)^{1.5}}, \qquad (1)$$

which is typical of a flux-limited sample with a magnitude cut at $i_{AB} < 24$. In equation (1) N_{gal} is a normalization related to the total number of galaxies per square degree under consideration.

2.1.1 Spectroscopic survey

Our benchmark spectroscopic survey has radial positions given by true redshifts (i.e. $\sigma_z = 0$ in the formulation below) and a redshift range $0.45 < z < 0.65$. Hence, for the 2D tomography of this survey we use top-hat bins[4] to compute angular power spectra. In Table 2 we show the different bin configurations considered, characterized by the number of bins in which we divide the survey volume and their width. Provided with the narrow redshift range we can assume that the bias does not evolve; hence we take $b = 2$ throughout.

Lastly, we discuss two cases for this survey, one where shot noise is non-negligible and another where it is a subdominant source of error. These cases are detailed in Table 1 and, for the redshift range under consideration, imply 9M and 40M galaxies, respectively (assuming full-sky surveys).

2.1.2 Narrow-band photometric survey

This case intends to be representative of a configuration such as the one proposed for the PAU survey where a set of narrow-band filters is expected to deliver 'low-resolution' spectra in a redshift range actually broader than the one considered here (Benítez et al. 2009; Gaztañaga et al. 2012). Hence, our narrow-band photo-z survey has accurate photometric redshifts of $\sigma_z = 0.004$, in the same redshift range of the spectroscopic case ($0.45 < z < 0.65$). The bias ($b = 2$) and the shot noise cases considered match those discussed in Section 2.1.1 (and are given in Table 1).

In turn the bin configurations assumed for the 2D tomography are also the same as for the spectroscopic survey given in Table 2, but with bin limits that now refer to photometric redshifts. Thus, the true redshift distribution of galaxies in each bin is no longer a top hat, but rather has a small overlap with the nearest-neighbouring bins due to the photo-z error, as described in equation (18) below. In the top panel of Fig. 1 we show this effect for the particular case of eight bins.

---

[1] www.pausurvey

[2] www.darkenergysurvey.org

[3] camb.info/sources

[4] To satisfy differentiability requirements at the edges we use in practice $\phi(z) \propto \exp[-((z - \bar{z})/(\Delta z/2))^{20}]$, where $\bar{z}$ is the mean redshift of the bin and Δz the full width.

Table 2. Bin configurations used for the 2D tomography in the case of the spectroscopic and the narrow-band photometric survey in a redshift range of $0.45 < z < 0.65$. We show the number of radial bins and their range of widths in redshift and comoving distance.

Number of bins	Δz	Δr (h^{-1} Mpc)
1	0.20	468
4	0.05	113–122
8	0.025	56–61
16	0.0125	28–31
20	0.010	22–25

Table 3. Bin configurations considered for a broad-band photometric survey within a redshift range $0.4 < z < 1.4$. We show the number of radial bins and their range of widths in redshift and comoving distance.

Number of bins	Δz	Δr (h^{-1} Mpc)
4	0.25	398–592
5	0.20	315–480
6	0.167	260–404
7	0.143	221–348
8	0.125	193–306
9	0.111	171–273
10	0.10	153–246

2.1.3 Broad-band photometric survey

On the other hand, we consider a photometric survey that uses broad-band filters such as DES (see Footnote 2), Pan-Starrs[5] or the future imaging component of *Euclid*.[6] These surveys are expected to achieve photometric redshift estimates with accuracies $\sigma_z \sim 5$ per cent/$(1 + z)$ (Banerji et al. 2008; Ross et al. 2011). In what follows we do not consider a possible redshift evolution of the photometric error but instead assume a conservative value of $\sigma_z = 0.1$.

Typically, optical photo-z surveys are fainter and sample a much larger number of galaxies than spectroscopic ones; hence, we assume a broader redshift range, $0.4 < z < 1.4$, and only a low shot noise case as given in Table 1. For the redshift range assumed this implies $\sim 150 \times 10^6$ galaxies. Table 3 shows the bin configurations we have considered for this case. While in the previous cases we have assumed that the bias is constant with redshift (because of the narrow-redshift range), for the broad-band photometric survey we introduce an evolution as follows (Fry 1996),

$$b(z) = 1 + (b_\star - 1)\frac{D(z_\star)}{D(z)}, \tag{2}$$

where $b_\star = 2$ is the bias at $z_\star = 1$. In turn for the evolution of bias we have always assumed the fiducial cosmology.

2.2 Spatial (3D) power spectrum

Since we are only interested in quasi-linear scales we assume the following simple model for the 3D galaxy power spectrum in redshift space:

$$P_g(k, \mu, z) = (b + f\mu^2)^2 \, D^2(z) \, P_0(k) \mathrm{e}^{-k^2\sigma_t^2(z)\mu^2}, \tag{3}$$

where P_0 is the linear spectrum at $z = 0$ (properly normalized), $D(z)$ is the linear growth factor, and the remaining amplitude depends on the bias $b(z)$ and the linear growth rate $f(z) \equiv \mathrm{d} \ln D/\mathrm{d} \ln a$. The Gaussian cut-off accounts for the fact that the radial information might be diluted due to photometric redshift errors σ_z.[7] In equation (3) this redshift error propagates to scales through $\sigma_t(z) = c\,\sigma_z/H(z)$. Note that σ_t depends also on the cosmic history. This should be taken into account when constraining relevant cosmological parameters (e.g. Ω_m).

For a spatial analysis the measured 3D power spectrum depends on the cosmological model assumed to convert redshift and angles
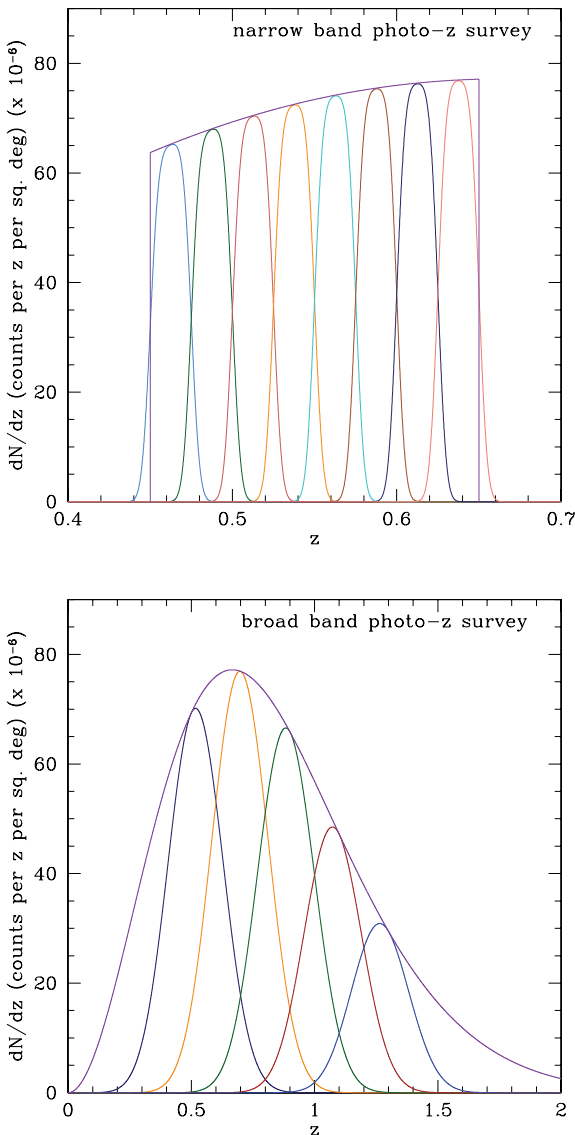

Figure 1. Top panel shows the redshift distribution in the spectroscopic and narrow-band photo-z survey (violet). For the narrow-band case we show how the true redshift distributions given by equation (1) look like if we divide the volume into eight consecutive redshift bins. The bottom panel also shows the same but for a broad-band photometric survey divided into five bins.

[5] pan-starrs.ifa.hawaii.edu
[6] www.euclid-imaging.net
[7] This expression is correct as long as the distribution of photometric errors is Gaussian, as we assume throughout this paper.

to distances. Hence, for every model to be tested against the data one must perform a new measurement. This process is very costly. Instead one can choose a *reference cosmological model* where the measurement is done once, and then transform the model prediction to this reference frame (Alcock & Paczynski 1979).

Let us call $P^{\mathrm{obs}}(k, \mu)$ the power spectrum measured in the *reference* cosmology and $P^{\mathrm{mod}}(\tilde{k}, \tilde{\mu})$ the model prediction at the point in cosmological parameter space being tested. The transformation of distances and angles from the cosmological model being tested $(\tilde{k}, \tilde{\mu})$ to those in the reference model (k, μ) is done through the scaling factors

$$c_\parallel = \frac{H(z)}{H^{\mathrm{mod}}(z)}; \quad c_\perp = \frac{d_{\mathrm{A}}^{\mathrm{mod}}(z)}{d_{\mathrm{A}}(z)}, \tag{4}$$

as $\tilde{k}_\parallel = k_\parallel/c_\parallel$ and $\tilde{k}_\perp = k_\perp/c_\perp$, where $\parallel$ indicates modes parallel to line of sight and $\perp$ perpendicular. The Hubble parameter and the angular diameter distances are given by

$$H(z) = 100 \, h \sqrt{\Omega_{\mathrm{m}}(1+z)^3 + \Omega_{\mathrm{DE}}(1+z)^{-3(1+w)}} \tag{5}$$

$$d_{\mathrm{A}}(z) = \frac{\int_0^z \frac{c \, \mathrm{d}z'}{H(z')}}{1+z}. \tag{6}$$

From the above, one trivially finds

$$\tilde{k} = k \sqrt{(1-\mu^2)c_\perp^{-2} + \mu^2 c_\parallel^{-2}} \tag{7}$$

$$\tilde{\mu} = \mu \, c_\parallel^{-1} / \sqrt{(1-\mu^2)c_\perp^{-2} + \mu^2 c_\parallel^{-2}}. \tag{8}$$

In addition the power spectrum is sensitive to the volume element. Thus, we must re-scale P^{mod} by the differential volume element with respect to the reference cosmology: $c_\perp^2 c_\parallel$. Lastly, following Tegmark (1997) and Seo & Eisenstein (2003) we construct χ^2 for each radial bin i as

$$\chi^2_{3\mathrm{D}}(i) = \int_{k_{\min}}^{k_{\max}} \frac{\mathrm{d}k k^2}{8\pi^2} \int_{-1}^1 \mathrm{d}\mu \, \mathrm{Cov}_{\mathrm{eff}}^{-1}(k, \mu) \left(P_{\mathrm{g}}^{\mathrm{obs}}(k, \mu, z_i) \right.$$
$$\left. - \frac{1}{c_\parallel c_\perp^2} P_{\mathrm{g}}^{\mathrm{mod}}(\tilde{k}, \tilde{\mu}, z_i) \right)^2, \tag{9}$$

where $\mathrm{Cov}_{\mathrm{eff}}^{-1}$ is defined for every bin i according to

$$\mathrm{Cov}_{\mathrm{eff}}^{-1}(k, \mu) = \int_{r_{\min}(i)}^{r_{\max}(i)} \mathrm{d}^3 r \left(\frac{\bar{n}(r)}{1 + \bar{n}(r) P_{\mathrm{g}}^{\mathrm{obs}}(k, \mu, \bar{z}_i)} \right)^2. \tag{10}$$

This is where the covariance of the power spectra is accounted for, which we assume to be diagonal in k. It has contributions from both sample variance and shot noise. In equations (9) and (10) P^{obs} is the measured spectra in the chosen reference cosmology which we take as our fiducial cosmological model introduced in Section 2.5.

For the spectroscopic survey we assume that bins are uncorrelated. Thus, the total χ^2 is given by

$$\chi^2_{3\mathrm{D}} = \sum_i \chi^2_{3\mathrm{D}}(i), \tag{11}$$

where the sum runs over all the bins considered.

2.3 Angular (2D) power spectrum

In our 2D analysis we consider the exact computation of the angular power spectrum of projected overdensities in a radial shell,

$$C_\ell^{ii} = \frac{2}{\pi} \int \mathrm{d}k \, k^2 P_0(k) \left(\Psi_\ell^i(k) + \Psi_\ell^{i,r}(k) \right)^2, \tag{12}$$

where

$$\Psi_\ell^i(k) = \int \mathrm{d}z \, \phi_i(z) b(z) D(z) j_\ell(kr(z)) \tag{13}$$

is the kernel function in real space and

$$\Psi_\ell^{i,r}(k) = \int \mathrm{d}z \, \phi_i(z) f(z) D(z) \left[\frac{2\ell^2 + 2\ell - 1}{(2\ell+3)(2\ell-1)} j_\ell(kr) \right.$$
$$- \frac{\ell(\ell-1)}{(2\ell-1)(2\ell+1)} j_{\ell-2}(kr)$$
$$\left. - \frac{(\ell+1)(\ell+2)}{(2\ell+1)(2\ell+3)} j_{\ell+2}(kr) \right] \tag{14}$$

should be added to Ψ_ℓ^i if we also include the linear Kaiser effect (Kaiser 1987; Fisher, Scharf & Lahav 1994; Padmanabhan et al. 2007). In turn, photo-z effects are included through the radial selection function $\phi(z)$, see below. This model then has the same assumptions as the 3D spectrum from equation (3).

Note that in equation (12) we are only considering density and RSD terms. We are neglecting General Relativity (GR) effects as well as velocity and lensing terms, which are in our cases subdominant to the ones considered. Nonetheless the framework of angular auto- and cross-correlations could easily include these effects when required (Bonvin & Durrer 2011; Challinor & Lewis 2011).

There are N_z angular power spectra, one per radial bin. But if we want to study all the clustering information we should add to our observables the $N_z(N_z - 1)/2$ cross-correlations between different redshift bins. These are given by

$$C_\ell^{ij} = \frac{2}{\pi} \int \mathrm{d}k \, k^2 P(k) \left(\Psi_\ell^i(k) + \Psi_\ell^{i,r}(k) \right) \left(\Psi_\ell^j(k) + \Psi_\ell^{j,r}(k) \right). \tag{15}$$

Therefore, we consider $N_z(N_z + 1)/2$ observable angular power spectra when reconstructing clustering information from tomography using N_z bins.

2.3.1 Radial selection functions

The radial selection functions ϕ_i in equations (12) and (15) are the probability to include a galaxy in the given redshift bin. Therefore, they are the product of the galaxy redshift distribution and a window function that depends on selection characteristics (e.g. binning strategy),

$$\phi_i(z) = \frac{\mathrm{d}N_{\mathrm{g}}}{\mathrm{d}z} W(z) \tag{16}$$

where $\mathrm{d}N_{\mathrm{g}}/\mathrm{d}z$ is given by equation (1). We consider two different $W(z)$ depending on the kind of redshift estimation. In a spectroscopic redshift survey $W(z)$ is a top-hat function with the dimensions of the redshift bin. On the other hand, if we include the effect of photo-z, then

$$W_i(z) = \int \mathrm{d}z_{\mathrm{p}} P(z|z_{\mathrm{p}}) W_i(z_{\mathrm{p}}), \tag{17}$$

where z_{p} is the photometric redshift and $P(z|z_{\mathrm{p}})$ is the probability of the true redshift to be z if the photometric estimate is z_{p}. For the photometric surveys we assume a top-hat selection $W(z_{\mathrm{p}})$ in photometric redshift and that $P(z|z_{\mathrm{p}})$ is Gaussian with standard deviation σ_z. This leads to

$$\phi_i(z) \propto \frac{\mathrm{d}N_{\mathrm{g}}}{\mathrm{d}z} \left(\mathrm{erf}\left[\frac{z_{\mathrm{p,max}} - z}{\sqrt{2}\sigma_z} \right] - \mathrm{erf}\left[\frac{z_{\mathrm{p,min}} - z}{\sqrt{2}\sigma_z} \right] \right), \tag{18}$$

where $z_{\mathrm{p,min}}$ and $z_{\mathrm{p,max}}$ are the (photometric) limits of each redshift bin considered. In the above equation and throughout this paper we assume that σ_z is constant in redshift.

2.3.2 Covariance matrix of angular power spectra

The covariance between the angular spectra of redshift bins ij and redshift bins pq is given by

$$\text{Cov}_{\ell,(ij)(pq)} = \frac{C_\ell^{\text{obs},ip} C_\ell^{\text{obs},jq} + C_\ell^{\text{obs},iq} C_\ell^{\text{obs},jp}}{N(\ell)}, \tag{19}$$

where $N(\ell) = (2\ell + 1)\Delta\ell f_{\text{sky}}$ is the number of transverse modes at a given ℓ and $\Delta\ell$ is typically chosen to make a Cov block diagonal (Cabré et al. 2007; Crocce, Cabré & Gaztañaga 2011a; Sobreira et al. 2011). For simplicity we consider an ideal full-sky survey and use $\Delta\ell = 1$ and $f_{\text{sky}} = 1$. In this way we avoid correlations between different modes in the covariance matrix, which is diagonal with respect to ℓ (which is consistent with the assumption that the 3D covariance is also diagonal in k).

Therefore, for each ℓ we define a matrix with $N(N + 1)/2$ elements, where N is the number of observables discussed in Section 2.3, to account for the covariances and cross-covariances of auto- and cross-correlations. In order to include observational noise we add to the auto-correlations in equation (19) a shot noise term,

$$C_\ell^{\text{obs},ij} = C_\ell^{ij} + \delta_{ij} \frac{1}{\frac{N_{\text{gal}}(j)}{\Delta\Omega}}, \tag{20}$$

that depends on the number of galaxies per unit solid angle included in each radial bin. We define χ_{2D}^2 assuming that the observed power spectrum C_ℓ^{obs} corresponds to our fiducial cosmological model discussed in Section 2.5, while we call C_ℓ^{mod} the one corresponding to the cosmology being tested,

$$\chi_{\text{2D}}^2 = \sum_\ell \left(C_\ell^{\text{obs}} - C_\ell^{\text{mod}} \right)^\dagger \text{Cov}_\ell^{-1} \left(C_\ell^{\text{obs}} - C_\ell^{\text{mod}} \right). \tag{21}$$

Note that each term in the sum is the product of $(N_z(N_z + 1)/2)$-dimensional vectors C_ℓ^{ij} where (ij) label all possible correlations of N_z redshift bins, and an $N_z(N_z + 1)/2 \times N_z(N_z + 1)/2$ matrix corresponding to their (inverse) covariance.

Recall that we use the exact calculation of C_ℓ using CAMB_SOURCES, rather than the well-known Limber approximation (Limber 1954).

2.4 Non-linear scales

Both χ_{3D} and χ_{2D} depend sensibly on the maximum k_{max} (or the minimum scale) allowed in the analysis. In this paper, we chose to fix k_{max} for all the bins and relate it to angular scales through $\ell_{\text{max}} = k_{\text{max}} r(\bar{z})$, where $\bar{z}$ is the mean redshift of the survey. In our fiducial cosmology we find $r(\bar{z}) = 1471 \, h^{-1} \, \text{Mpc}$ in the redshift range $0.45 < z < 0.65$ and $r(\bar{z}) = 2219 \, h^{-1} \, \text{Mpc}$ when $0.4 < z < 1.4$. In addition, we do not consider a dependence of ℓ_{max} on redshift (i.e. same ℓ_{max} for all redshift bins and their cross-correlation).

For the largest scale we use $k_{\text{min}} = 10^{-4} \, h \, \text{Mpc}^{-1}$ in the 3D analysis and $\ell_{\text{min}} = 2$ in the angular case. We have not found any significant dependence on k_{min} or ℓ_{min}.

2.5 Cosmological model and growth history

We assume the underlying cosmological model to be a flat Λ cold dark matter (ΛCDM) universe with cosmological parameters $w = -1$, $h = 0.73$, $n_s = 0.95$, $\Omega_{\text{m}} = 0.24$, $\Omega_{\text{b}} = 0.042$ and $\sigma_8 = 0.755$. These parameters specify the cosmic history as well as the linear spectrum of fluctuations P_0. In turn, the growth rate can be well approximated by

$$f(z) \equiv \Omega_{\text{m}}(z)^\gamma \tag{22}$$

and $\gamma = 0.545$ for ΛCDM. Consistently with this we obtain the growth history as

$$D(z) \equiv \exp\left[-\int_0^z \frac{f(z)}{1+z} \text{d}z \right] \tag{23}$$

(where D is normalized to unity today). The parameter γ is usually employed as an effective way of characterizing modified gravity models that share the same cosmic history as GR but different growth history (Linder 2005). In part of our analysis we focus on ΛCDM models and assume the GR value $\gamma = 0.545$. We deviate from this in Section 3.1.2 where we take γ as a free parameter independent of redshift.

2.6 Likelihood analysis

In order to find constraints on cosmological models we integrate over the space of parameters defining the model, finding the value of the likelihood given by

$$-2\log\mathcal{L} \propto \chi^2, \tag{24}$$

where we approximate the likelihood as Gaussian in the power spectra. Given the prior ϑ on the parameters one defines a probability for each sampled point i in parameter space given by

$$\mathcal{P}(i) \propto \mathcal{L}(i) \times \vartheta(i). \tag{25}$$

Finally, the mean and covariance matrix of the parameters are obtained from

$$\bar{p}_a = \sum_i \mathcal{P}(i) p_a(i) \tag{26}$$

$$\Sigma_{(p_a, p_b)} = \sum_i \mathcal{P}(i)(p_a(i) - \bar{p}_a)(p_b(i) - \bar{p}_b), \tag{27}$$

where $p_a(i)$ is the value of the parameter a in the grid point i, $\bar{p}_a$ is the mean value and $\Sigma_{(p_a, p_b)}$ is the covariance between parameters a and b. In equations (26) and (27), $\mathcal{P}(i)$ is normalized to unity over the grid. In addition we assume flat priors.

By construction the likelihood peaks at the fiducial value considered in the analysis. In all our studies we have chosen wide prior limits and therefore have found no dependence on these limits, but find that the mean agrees with the fiducial value and the posteriors are quite Gaussian. Then in the case of only one nuisance parameter p, solving $\chi^2(p) - 1 = 0$ gives the same variance as likelihood sampling which allows us to speed up constraints considerably.

2.7 Figures of merit

We consider two different analyses in order to compare 3D clustering with 2D tomography including all the auto- and cross-correlations between redshift bins.

On the one hand, a *bias fixed case*, in which we only vary Ω_{m} (which affects both the shape and the amplitude of the power spectrum, and can be constrained as if we had good knowledge of the bias prior to the analysis).

On the other hand, we consider a *bias free case*, in which only b and γ (hence f through equation 22) are allowed to vary. This changes the (anisotropic) amplitude of the power spectrum, but not the underlying shape. This case is virtually the same as the standard analysis of RSD (Cabré & Gaztañaga 2009; White, Song & Percival 2009; Ross et al. 2011). For this case we had to adapt CAMB_SOURCES slightly, see the discussion in Appendix A.

To make the comparison quantitative we define a FoM based on the covariance matrix Σ,

$$\text{FoM}_S = \sqrt{\frac{1}{\det[\Sigma]_S}}, \qquad (28)$$

where S is the subspace of parameters we are interested in. If this subspace corresponds to only one parameter, then the FoM is the inverse of the square root of the variance of the corresponding parameter. Thus, we have the following cases.

(i) FoM_{Ω_m}: constraints on Ω_m, with other parameters fixed at fiducial values.

(ii) FoM_b and FoM_γ: bias and γ constraints when marginalized over γ and bias, respectively. Other parameters are fixed at their fiducial values.

(iii) $\text{FoM}_{b\gamma}$: joint constraint on bias and γ, with other parameters fixed at fiducial values.

3 RESULTS

In this section we present the forecasts on Ω_m (*bias fixed*) and b and γ (*bias free*) from the measurement of either spatial or angular power spectra in the spectroscopic survey described in Section 2.1.1. Next we perform the *bias fixed* analysis in the narrow-band photometric survey with accurate photo-z discussed in Section 2.1.2

and the broad-band photometric survey defined in Section 2.1.3. Note that despite photometric redshift errors large-scale RSD can be measured in photometric surveys for binned data (Nock, Percival & Ross 2010; Crocce et al. 2011b), albeit with possible large error bars. Nonetheless for photometric surveys we concentrate on the *bias fixed* case only.

All the analyses introduced above have been done for three different $k_{max} = \{0.05, 0.1, 0.2\}\, h\,\text{Mpc}^{-1}$ (with corresponding ℓ_{max} as detailed in Section 2.4) and several bin configurations (see Tables 2 and 3). We then study for which redshift bin width the information obtained using angular power spectra (quantified by the FoM in Section 2.7) is similar to that derived from the 3D power spectra.

3.1 Spectroscopic redshifts

3.1.1 Bias fixed case

The top panels of Fig. 2 show the FoM on Ω_m for different k_{max} and $\ell_{max} = r(\bar{z})\, k_{max}$ as a function of the number of redshift bins N_z in which we divide the full survey volume (see Table 2). Here, the dashed lines are results from fitting the 3D power spectrum according to equations (9) and (11), while the solid lines are from the 2D tomography including all the auto- and cross-correlations of
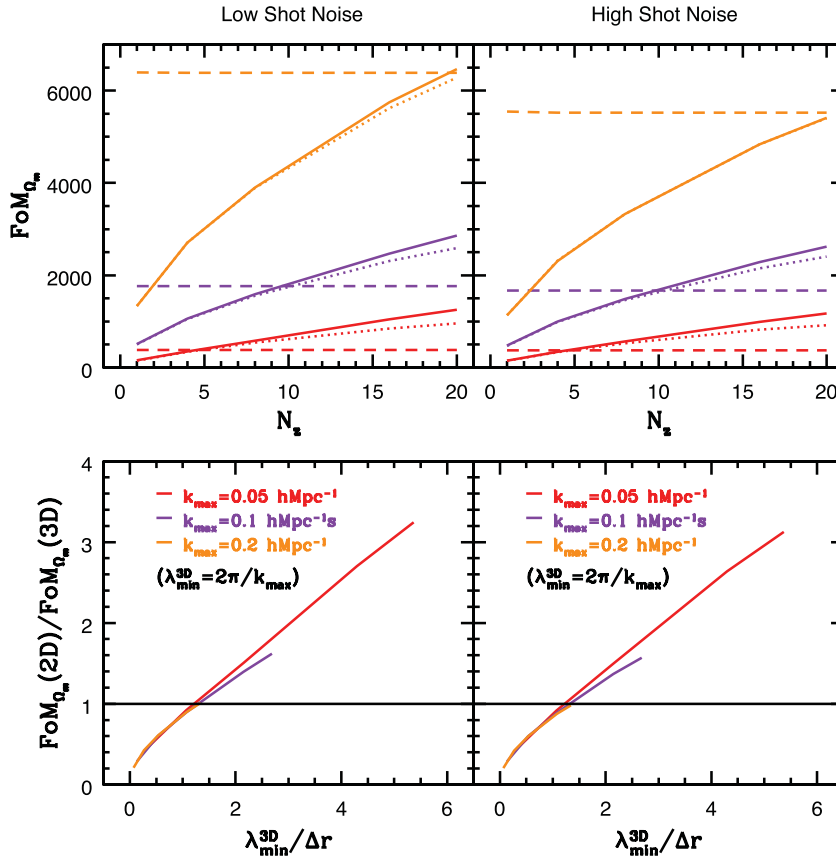

Figure 2. Spectroscopic survey and bias fixed: the top panels show FoM_{Ω_m}(2D) and FoM_{Ω_m}(3D) as a function of the number of bins in which we divide the survey for the analysis (left-hand panel for a low shot noise survey and the right for a high shot noise survey). The dashed line corresponds to the 3D analysis, dotted to the 2D tomography using only auto-correlations and solid to auto- plus cross-correlations. Different colours correspond to different minimum scales, as detailed in the bottom panel inset labels. The bottom panels show the ratio of FoM_{Ω_m}(2D) (auto plus cross) and FoM_{Ω_m}(3D) as a function of the bin width Δr normalized by the minimum scale assumed in the 3D analysis. Remarkably the recovered constraints from full tomography match the 3D ones for $\Delta r \sim \lambda_{min}^{3D}$ for all λ_{min}^{3D}. We note that different lines in the bottom panels are truncated differently merely because we have done the analysis for the three k_{max} cases down to the same minimum Δr.

bins, as in equation (21). The left (right) panel corresponds to the low (high) shot noise case as defined in Table 1.

As expected we find that the FoM increases for increasing k_{max}, ℓ_{max}. Including more modes to χ^2 adds more information to our analysis and therefore results in better constraints. We also see that FoM$_{\Omega_m}$ from the 3D analysis only shows a marginal dependence on the bin configuration. This is because χ^2 per redshift bin is roughly proportional to the volume of the redshift shell, see equation (9). Thus, increasing the number of bins at the expense of decreasing their volume keeps FoM$_{\Omega_m}$ unchanged. We obtain the same result for all the cases studied in this paper, as long as P_g does not change abruptly with redshift. Thus, from now on we will only refer to the 3D results in the whole survey.

This picture changes for the 2D tomography. Here, the transverse information is fixed once ℓ_{max} is set ($2\ell + 1$ modes per ℓ value up to ℓ_{max}). As we increase the number of narrower bins N_z (with the fixed total redshift range) we have several effects.

(i) Decreasing the number of galaxies per bin increases the shot noise per bin.

(ii) Increasing the number of bins so that they are thinner proportionally increases the signal auto power spectrum in each bin (there is less signal power suppression due to averaging along the radial direction).

(iii) When we split a wide redshift bin into two, we double the number of angular auto power spectra (transverse modes). This results in a larger FoM because the signal-to-noise ratio in each bin remains nearly constant (both the shot noise and signal in each bin increase proportionately). This gain is illustrated by the dotted line in Fig. 2, which corresponds to the FoM produced by just using auto-correlations. For even narrower redshift bins the bins will become correlated and the gain will saturate, but this is not yet the case in our results as the redshift bins are still large compared to the clustering correlation length. In the limit in which all modes of interest are very small compared to the shell thickness and they are statistically equivalent, for a single power spectrum amplitude parameter one expects FoM $= 1/\sigma \propto \sqrt{N_z}$, as obtained in Fig. 2 for low N_z.[8]

(iv) When we increase the number of narrower bins, we also include information of radial modes by adding the cross-correlation between different redshift bins (illustrated by the solid line in Fig. 2 that corresponds to the total FoM from auto- plus cross-correlations). Note how adding the cross-correlations to the auto-correlations (solid lines in Fig. 2) only increases the FoM moderately as compared to the auto-correlation result (dotted line). This reflects the fact that there are fewer radial modes than transverse ones, while much of the Ω_m constraint comes from the shape of $P(k)$ that is isotropic.

(v) As shown in Fig. 2, the 2D FoM can exceed the 3D FoM. This happens because the 3D analysis is limited by construction to a maximum number of modes, given by k_{max}, while in 2D we only limit the analysis to $\ell < \ell_{max}$ and we can formally exceed the maximum number of narrow redshift bins, as explained in points (ii) and (iii) above. But in reality, these additional modes are not necessarily independent and they could well be in the non-linear regime, so it is not clear to what extent we can use them to increase

the FoM. As we want to restrict our analysis to $k < k_{max}$ we should not use redshift bins that are smaller than λ_{min}^{3D}.

The bottom panels of Fig. 2 show the ratio of the 2D and 3D FoMs against the bin width (instead of N_z), now normalized by the minimum scale used in the 3D analysis, $\lambda_{min}^{3D} = \frac{2\pi}{k_{max}}$ (for three different k_{max} as before). We find FoM(2D) $\sim$ FoM(3D) when $\lambda_{min}^{3D} \sim \Delta r$ for all λ_{min}^{3D}. More precisely,

$$\Delta r = c\Delta z/H(z) \simeq 0.8\lambda_{min}^{3D}. \tag{29}$$

Basically, this means that the 3D clustering information is recovered once the binning is such that the radial bin width equals the minimum scale probed in the 3D analysis. In this case one is able to constrain the parameters without loss of information compared to a 3D analysis, though the actual range of scales around k_{max} that are used in the 2D analysis may be slightly different from the ones used in the 3D analysis.

Note that as mentioned in point (v) above, we can only really trust our results for the 2D FoM up to the limit in which they are equal to or smaller than the 3D FoM, i.e. in the range in which the width of redshift bins is greater than or similar to λ_{min}^{3D}. To use the smaller scales we first need to explore to what extent we can model the non-linear 2D clustering to improve the FoM. We are currently investigating this issue (Asorey et al., in preparation).

Lastly, note that including shot noise does degrade the FoM as shown in the right-hand panel of Fig. 2. However, this does not change the above conclusions.

3.1.2 Bias free case

We now turn to the *bias free* case where we assume that we know perfectly the shape of the power spectrum so that all the parameters are fixed at their fiducial values except the bias b and the growth index γ.

In Fig. 3 we plot the combined FoM obtained for the bias b and growth index γ, and the FoM of each of these two parameters marginalized over the other, as a function of the number of redshift bins considered in the analysis (for a fixed survey redshift range $0.45 < z < 0.65$). As in Fig. 3, the dashed line corresponds to the 3D analysis, dotted line to the 2D tomography using only auto-correlations[9] and solid line to the full 2D case where we add auto- and cross-angular correlations.

We find a similar trend for the evolution of the different FoMs of the γ and b parameters (either combined or marginalized) to when varying Ω_m. Constraints given by the spatial power spectrum are stable, while constraints from the projected power spectrum in the bins increase with the number of bins into which we divide the survey. However, there is a substantial difference in regard to the contribution of radial modes. Now the contribution of cross-correlations is very large (compare the solid lines to the dotted lines in the left-hand panel of equation 19). In fact, without cross-correlations we do not recover all the 3D information. This is because RSD information (i.e. our *bias free case*) is based on the relative clustering amplitude of modes parallel and transverse to the line of sight. The contribution from radial modes is much more evident for the γ constraint (FoM$_\gamma$ and then FoM$_{b\gamma}$) because γ is basically what quantifies this relative clustering amplitude (in addition $f \equiv \Omega(z)^\gamma$ depends on redshift while we assume that bias does not).

---

[8] A similar effect can be seen in figs 8 and 9 of Ross et al. (2011) in the context of RSD constraints in a broad-band photometric survey. In their fig. 8 the constraint in $f\sigma_8$ saturates when they consider only one redshift bin. However, the error on $f\sigma_8$ from the combined measurements on several bins does not saturate (fig. 9).

[9] We note that we refer here to observables. The covariance of the auto-correlations does include cross-correlations of redshift bins, see equation (19).
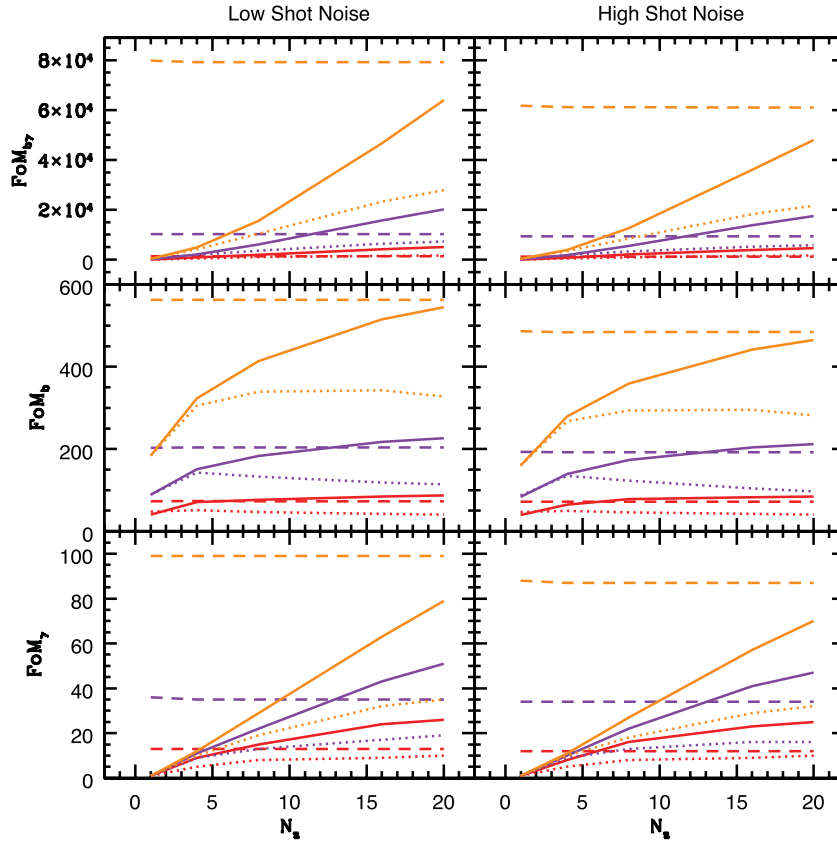
Figure 3. Spectroscopic survey and bias free: the top panels show the combined $b-\gamma$ constraint resulting from 3D clustering (dashed lines) or 2D tomography considering as observables only auto-correlations in redshift bins (dotted lines), or adding to this the cross-correlations (solid lines). The x-axis corresponds to the number of radial bins considered in the analysis. Different colours label different minimum scales assumed (same values and labels as in Fig. 2). The middle and bottom panels correspond to individual b or γ constraints after marginalization over γ or b, respectively. As for the *bias fixed* we find that 3D information can be recovered but now the role of radial modes is much more important because RSD (our *bias free* case) relies on the relative clustering amplitude of radial and transverse modes.

As we have done with FoM_{Ω_m} we show in Fig. 4 the dependence of the ratios between 2D and 3D FoM on $\lambda_{\min}^{3D}/\Delta r$. We find that both analyses produce the same constraints when the mean redshift bin width is slightly smaller than $\lambda_{\min}^{3D}$ (and we use auto- and cross-2D correlations). Comparing these results with the *bias fixed* case, it seems that for the RSD probe we need to extract more radial information. In this case

$$\Delta r = c\Delta z/H(z) \simeq 0.6\,\lambda_{\min}^{3D} \qquad (30)$$

as compared to 0.8 in equation (29). This means that we have to include more radial bins when developing the fit to angular correlations than when only fitting Ω_m if we want to match the constraints from 3D clustering. This in practice corresponds to using slightly narrower redshift bins. This may also result in more information being included from radial modes with $k > k_{\max}$, though a detailed analysis of the implications of this is beyond the scope of the current paper.

3.2 Photometric redshifts

In this section we show how the results found in the previous section extend to the photometric surveys detailed in Sections 2.1.2 and 2.1.3. For concreteness we will only consider the *bias fixed* study where all cosmological parameters are fixed at their fiducial values except for Ω_m.

3.2.1 Narrow-band photometric survey (PAU-like)

In the top panels of Fig. 5 we show the Ω_m constraints (*bias fixed* case) from the 3D and 2D analysis (dashed and solid lines, respectively) in a narrow-band photometric survey with $\sigma_z = 0.004$. In the bottom panels we show how the ratio between 2D and 3D FoMs depends on the ratio between the minimum scale of the 3D analysis and the mean comoving width of radial shells.

We find basically the same result as in the spectroscopic survey. Constraints from a projected or unprojected analysis are equivalent when the mean width of the radial shells (set by our binning strategy) is equal to the minimum scale considered in the 3D analysis $\lambda_{\min}^{3D}$. The absolute value of each FoM is degraded with respect to the FoM reached with a spectroscopic survey because photo-z errors dilute the clustering in the radial direction. This broadens the selection functions in the 2D analysis and introduces a cut-off already at quasi-linear scales in the 3D $P(k)$. In both cases the consequence is that the signal-to-noise ratio reduces and thus errors of observables degrade. But if we compare Figs 2 and 5, we see that the spectroscopic survey and a photometric one with very accurate redshifts are almost indistinguishable in terms of bin width optimization.

3.2.2 Broad-band photometric survey (DES-like)

We now consider a deep survey ($i_{AB} < 24$) with redshifts estimated by photometry with broad-band filters ($\sigma_z = 0.1$), and use the full
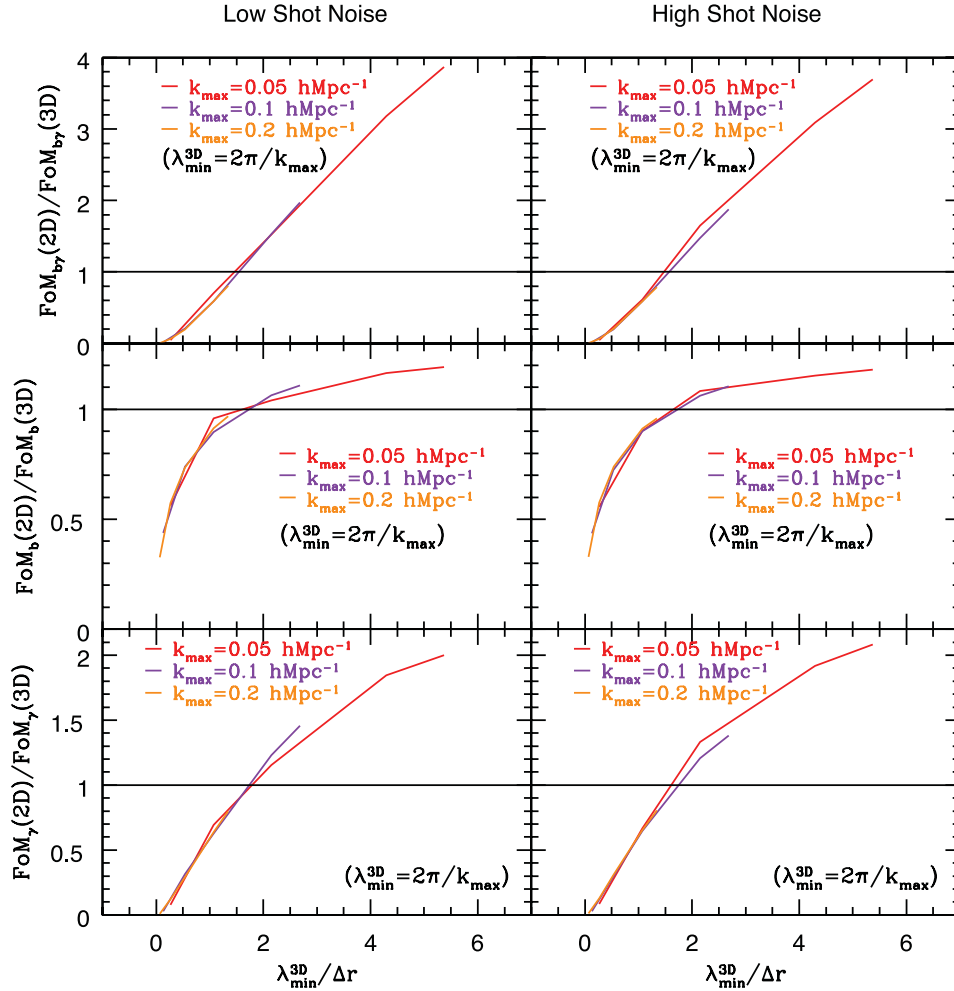
Figure 4. Spectroscopic survey and bias free: the top panels show the ratio between combined $FoM_{b\gamma}$ (2D) (auto- plus cross-correlations) and $FoM_{b\gamma}$ (3D) with respect to $\lambda_{min}^{3D} = 2\pi/k_{max}$, normalized by the mean width of the redshift bins Δr in the analysis. The middle and bottom panels show the same but for ratios of FoM_b and FoM_γ, respectively. We show results for low shot noise and high shot noise in the left- and right-hand panels, respectively. To reconstruct RSD information in practice, one needs bins slightly smaller than λ_{min}^{3D}.

catalogue with $0.4 < z < 1.4$. We obtain the FoM for Ω_m shown in the top-left panel of Fig. 6.

Now the large photo-z error removes most of the radial information; thus, all FoM_{Ω_m} are degraded with respect to spectroscopic and narrow-band photometric surveys. In addition, we find that FoM_{Ω_m} saturates with the number of redshift bins included in the survey for every k_{max}. This effect is produced by the overlapping between true galaxy distributions at different bins induced by photo-z transitions.

We also find that the configuration in which spatial and projected analysis constrain Ω_m equally corresponds to the same number of bins for all the k_{max} considered. Therefore, as we can see in the bottom-left panel of Fig. 6, the scale given by λ_{min}^{3D} is not ruling the dependences. Instead it is the scale of the photometric redshifts which is affecting both clustering analyses. This is shown in the right-hand panel of Fig. 6 where we plot the ratio of FoMs (2D versus 3D) against a new scaling: $\sigma_r/\Delta r$. We find that for a DES-like case, with the assumption of $\sigma_z = 0.1$, one needs roughly five bins for the 2D tomography to optimally recover the 3D clustering information. This corresponds to

$$\Delta z \simeq 2\sigma_z. \tag{31}$$

With a lower σ_z the number of bins will increase.

4 CONCLUSIONS

In this paper we have studied the redshift bin width that allows us to recover the full 3D clustering constraints from tomography of angular clustering (i.e. the combination of all the auto- and cross-correlations of redshift bins). We explore three surveys with different properties: a spectroscopic and a narrow-band photometric survey in the redshift range $0.45 < z < 0.65$, and a deeper broad-band photometric survey that covers redshifts in the range $0.4 < z < 1.4$. We have considered how well we can recover the shape of the power spectrum by allowing Ω_m to be free and fixing the amplitude of clustering, including bias. We call this the *bias fixed* case. We have also explored how to recover the information from RSD, by measuring the *anisotropic* amplitude of the power spectrum allowing for both a free bias and a free growth index. This is the *bias free* case. We restrict our study to quasi-linear scales and we consider only the scales above some minimum scale $\lambda_{min}^{3D} = 2\pi/k_{max}$, where $k < k_{max}$ and k_{max} is either 0.05, 0.1 or $0.2 \, h \, Mpc^{-1}$. In angular space this corresponds to $\ell < \ell_{max} \simeq k_{max} r(z)$, where $r(z)$ is the radial distance to the mean redshift bin.

The 3D analysis has almost no dependence on the number of redshift bins because radial modes are already included in each bin. In contrast, the 2D tomographic analysis depends strongly on the
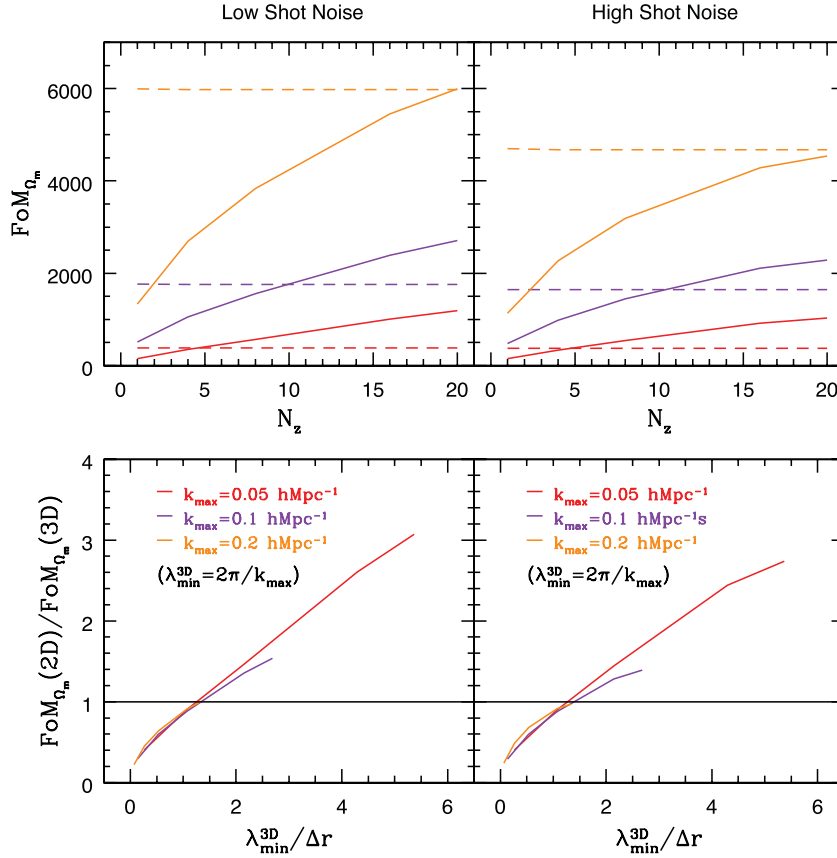
Figure 5. Narrow-band photometric survey (PAU-like) and bias fixed: the top panels show FoM_{Ω_m} (2D) (auto- plus cross-correlations) and FoM_{Ω_m} (3D) with respect to the number of bins for $k_{max} = \{0.05, 0.1, 0.2\}\, h\,\mathrm{Mpc}^{-1}$ (red, violet and orange colours). We plot 2D FoMs with solid lines and 3D FoMs with dashed lines. The bottom panels show the ratio between both FoMs with respect to the minimum scale used in the 3D analysis, $\lambda_{min}^{3D} = 2\pi/k_{max}$, divided by the mean width Δr of the redshift bin. We conclude that we get similar constraints from 2D and 3D analysis when Δr is close to λ_{min}^{3D} and that in terms of bin width optimization the spectroscopic and photometric analysis are almost identical.

number of bins (or equivalently on redshift bin widths), since broad bins average down transverse power on scales smaller than the bin width, and it is only by using multiple thin shells that radial modes are included.

For the *bias fixed* case in the spectroscopic survey we have found that we recover all the information with 2D tomography when the width of the redshift bins that we use to do the tomography is similar to the minimum scale used in the 3D observables, λ_{min}^{3D}. More precisely we find that the optimal bin width is (see Fig. 2 and equation 29) $\Delta r = c\Delta z/H(z) \simeq 0.8\,\lambda_{min}^{3D}$. In addition most of the 2D constraints come from auto-correlations.

When studying RSD, i.e. in the *bias free* case, we see that if we want to recover the 3D constraints we need radial shells which are slightly smaller, i.e. $\Delta r \simeq 0.6\lambda_{min}^{3D}$ (see Fig. 4), which means that we would need more bins than in the case in which we just want to measure the shape of $P(k)$. In addition, we find it necessary to include in the observables the cross-correlation between redshift bins. This is expected because in the RSD case we are comparing the clustering in the radial and transverse direction to the line of sight: information from radial modes should be more important than in the case in which we just study information in the isotropic shape of the power spectrum. We also note how we cannot recover the 3D information from RSD when we just use auto-correlations (see the dotted line in Fig. 3).

We found that in the *bias fixed* case, the narrow-band photometric survey is almost equivalent to a spectroscopic survey, and we therefore reach the same conclusions with respect to the optimal bin width for the tomography of galaxy counts. In the case of a deeper broad-band photometric survey we find that the typical uncertainty in photometric redshifts σ_z severely limits the accuracy of the radial information for both 3D and 2D cases. In this case the information recovery does not depend strongly on λ_{min}^{3D}, because this is smaller than the scale corresponding to the photometric redshift accuracy, i.e. $c\,\sigma_z/H(z) > \lambda_{min}^{3D}$. The optimal redshift bin width in this case is simply given by $\Delta z \simeq 2\sigma_z$.

For a redshift range $0.4 < z < 1.4$ and $\sigma_z = 0.1$ (DES-like survey) we find that we will need only five redshift bins to constrain Ω_m using tomography with a similar precision to a full 3D analysis of the survey. In comparison, for a PAU-like survey with $\sigma_z \simeq 0.004$ and $k_{max} = 0.1$ we need about 44 redshift bins of width $\Delta z \simeq 0.023$ each.

We conclude from our analysis that it seems possible to recover the full 3D clustering information, including RSD information, from 2D tomography. This has the disadvantage of needing a potentially large number of redshift bins, and correspondingly large covariance matrices between observables. But it has the great advantage of simplifying the combination with WL and of just using observed quantities, i.e. angles and redshifts, avoiding the use of a fiducial cosmology to convert angles and redshifts into 3D comoving
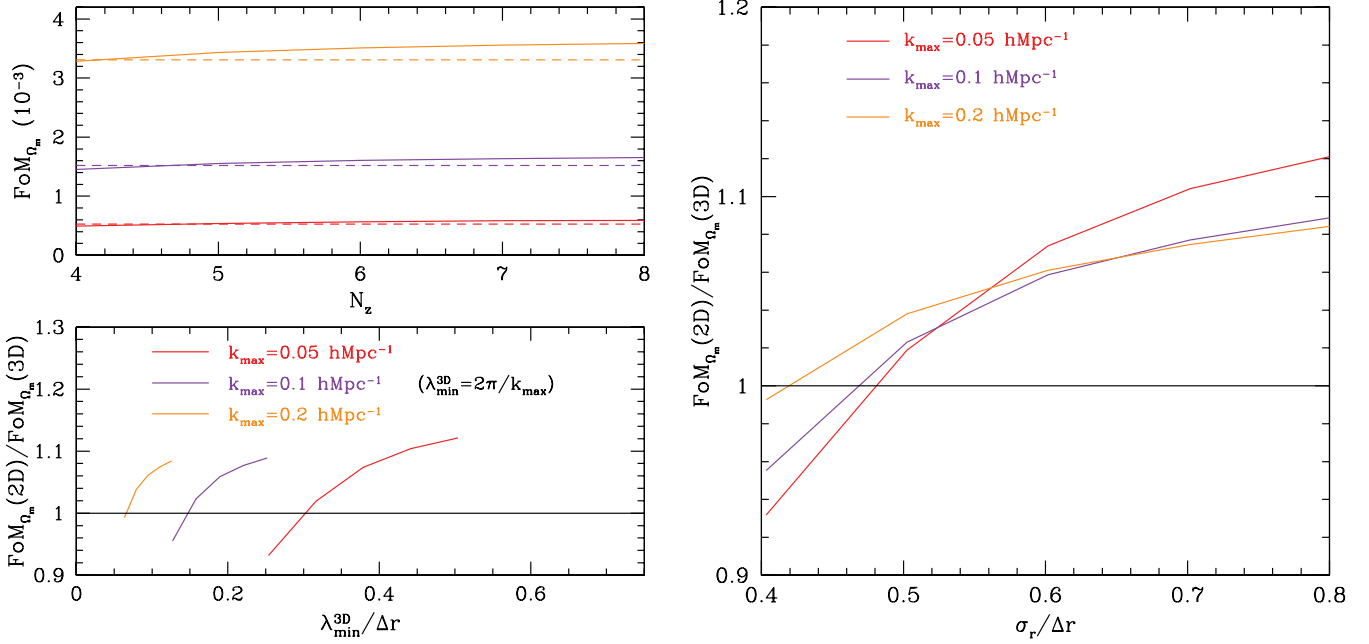
Figure 6. Broad-band photometric survey (DES-like) and bias fixed: the top-right panel shows FoM_{Ω_m} (2D) and FoM_{Ω_m} (3D) with respect to the number of bins N_z used in the analysis, for $k_{\max} = \{0.05, 0.1, 0.2\}\, h\,\text{Mpc}^{-1}$ (red, violet and orange colours, respectively). 2D FoMs are plotted with solid lines and 3D with dashed lines, and we only consider low shot noise. The bottom-left panel shows the ratio of both FoMs with respect to $\lambda_{\min}^{3D} = 2\pi/k_{\max}$ divided by Δr. The equivalence of the recovered FoM now changes for different $k_{\max}$. However, when this ratio is plotted with respect to the comoving scale of photo-z, σ_r (normalized by Δr), the different $\lambda_{\min}$ lines cross each other for $\Delta r \sim 2\sigma_r$. This implies that it is the relative values of Δr and σ_r what set the equivalence of 3D and 2D tomography. In particular, for a DES-like survey one recovers the 3D constraints from 2D analysis using five redshift bins.

coordinates. In practice, probably both types of analysis should be used to seek for consistency.

REFERENCES

Alcock C., Paczynski B., 1979, Nat, 281, 358
Banerji M., Abdalla F. B., Lahav O., Lin H., 2008, MNRAS, 386, 1219
Benítez N. et al., 2009, ApJ, 691, 241
Blake C., Collister A., Bridle S., Lahav O., 2007, MNRAS, 374, 1527
Bonvin C. R., Durrer R., 2011, Phys. Rev. D, 84, 063505
Cabré A., Gaztañaga E., 2009, MNRAS, 393, 1183
Cabré A., Fosalba P., Gaztañaga E., Manera M., 2007, MNRAS, 381, 1347
Cai Y. C., Bernstein G., 2012, MNRAS, 422, 1045, preprint (arXiv:1112.4478)
Casas R. et al., 2010, Proc. SPIE, 7735, 773536
Challinor A., Lewis A., 2011, Phys. Rev. D, 84, 043516
Crocce M., Cabré A., Gaztañaga E., 2011a, MNRAS, 414, 329

Crocce M., Gaztañaga E., Cabré A., Carnero A., Sánchez E., 2011b, MN-RAS, 417, 2577
Fisher K. B., Scharf C. A., Lahav O., 1994, MNRAS, 266, 219
Fry J. N., 1996, ApJ, 461, L65
Gaztañaga E., Eriksen M., Crocce M., Castander F. J., Fosalba P., Marti P., Miquel R., Cabré A., 2012, MNRAS, 422, 2904
Kaiser N., 1987, MNRAS, 227, 1
Kitching T. D., Heavens A. F., Miller L., 2011, MNRAS, 413, 2923
Komatsu E. et al., 2011, ApJS, 192, 18
Lewis A., Challinor A., 2007, Phys. Rev. D, 76, 083005
Lewis A., Challinor A., Lasenby A., 2000, ApJ, 538, 473
Limber D. N., 1954, ApJ, 119, 655
Linder E. V., 2005, Phys. Rev. D, 72, 043529
Montanari F., Durrer R., 2012, Phys. Rev. D, 86, 063503
Nock K., Percival W. J., Ross A. J., 2010, MNRAS, 407, 520
Padmanabhan N. et al., 2007, MNRAS, 378, 852
Ross A. J., Percival W. J., Crocce M., Cabré A., Gaztañaga E., 2011, MN-RAS, 415, 2193
Seo H., Eisenstein D. J., 2003, ApJ, 598, 720
Sobreira F., 2011, Phys. Rev. D, 84, 103001
Tegmark M., de Simoni F., Rosenfeld R., da Costa L. A. N., Maia M. A. G., Makler M., 1997, Phys. Rev. Lett., 79, 3806
Thomas S. A., Abdalla F. B., Lahav O., 2011, MNRAS, 412, 1669
White M., Song Y.-S., Percival W. J., 2009, MNRAS, 397, 1348

APPENDIX A: MODIFYING CAMB_SOURCES TO SAMPLE GROWTH RATE AND BIAS

In order to consider the *bias free* case we had to modify CAMB_SOURCES to accept as (independent) inputs bias and growth rate (parametrized through γ as in equation 22). In addition, this case does not involve changes in the shape of the real space spectrum; thus, one should be able to sample parameter space without

the need to compute the transfer functions at each point of parameter space.

To fulfil these needs we have factorized the terms in our observables that depend on the cosmic history (for our reference cosmology) from those that depend on the bias b and growth index γ. The factorization in the case of auto- and cross-correlation is given by

$$C_\ell^{ii} = b_i^2 C_\ell^{ii\,(0)} + 2b_i f_i C_\ell^{ii\,(2)} + f_i^2 C_\ell^{ii\,(4)} \qquad (A1)$$

$$
\begin{aligned}
C_\ell^{ij} = {} & b_i b_j C_\ell^{ij\,(0)} + b_i f_j C_\ell^{ij\,(2)} \\
& + b_j f_i C_\ell^{ij\,(2')} + f_i f_j C_\ell^{ij\,(4)},
\end{aligned} \qquad (A2)
$$

where b_i is the bias of the bin i and f_i is the growth rate given by equation (22), evaluated at the mean redshift of the bin i. This factorization assumes that $f(z)$ does not vary much within the redshift range of the bin (neither b). We have tested this assumption using the exact CAMB_SOURCES evaluation or the reconstruction of equations (A1) and (A2) and found an excellent match for the bin widths considered in this paper.

Using the observed C_ℓ and solving a linear set of equations using different values for b_i we can store the value of $C_\ell^{ii\,(2)}$, $C_\ell^{ij\,(2)}$, $C_\ell^{ij\,(2')}$, $C_\ell^{ii\,(4)}$ and $C_\ell^{ij\,(4)}$. The values of $C_\ell^{ii\,(0)}$ and $C_\ell^{ij\,(0)}$ are obtained by excluding RSD in C_ℓ. Then, we sample b and γ space using these factors and the reconstruction given by equations (A1) and (A2) obtaining C_ℓ^{mod} in parameter space.

In the reconstruction we assume the underlying value of $\Omega_{\mathrm{m}} = 0.24$ given by our reference cosmology while the growth factor $D(z)$ is included in the integrals that are contained in the cosmic history-dependent factors $C_\ell^{ij\,(n)}$.

This paper has been typeset from a T<small>E</small>X/L<small>A</small>T<small>E</small>X file prepared by the author.